Electrochimica Acta 388 (2021) 138527

Contents lists available at ScienceDirect

Electrochimica Acta

journal homepage: www.elsevier.com/locate/electacta

The impact of fiber arrangement and advective transport in porous electrodes for silver-based thermally regenerated batteries

Nicholas R. Cross[a], Derek M. Hall[b,c], Serguei N. Lvov[b,c,d], Bruce E. Logan[a,e], Matthew J. Rau[f,*]

[a] Department of Chemical Engineering, Pennsylvania State University, University Park, PA 16802, United States
[b] The EMS Energy Institute, Pennsylvania State University, University Park, PA 16802, United States
[c] Department of Energy and Mineral Engineering, Pennsylvania State University, University Park, PA 16802, United States
[d] Department of Materials Science and Engineering, Pennsylvania State University, University Park, PA 16802, United States
[e] Department of Civil and Environmental Engineering, Pennsylvania State University, University Park, PA 16802, United States
[f] Department of Mechanical Engineering, Pennsylvania State University, University Park, PA 16802, United States

ARTICLE INFO

Article history:
Received 14 December 2020
Revised 27 April 2021
Accepted 28 April 2021
Available online 14 May 2021

Keywords:
Thermally regenerative battery
Electrodeposition uniformity
Advective mass transport
Vortex generation
Porous electrode structure

ABSTRACT

The silver-based thermally regenerative ammonia battery is a new technology for converting low-grade waste heat (<100 °C) to electrical power. These hybrid flow batteries are charged using energy derived from waste heat, rather than electrical power, and can be cycled hundreds of times without a decrease in performance. Design factors that impact operational conditions and performance are needed to improve reliability and increase power densities. For example, the structure of the porous electrodes could alter silver deposition rates and porosities of the electrodes during operation, leading to preferential flow paths from clogging of pores that would impact cycle longevity and power. A 2D numerical model was therefore used to study the relationship between fluid flow and electrodeposition in the porous electrodes using cylinders in cross-flow to represent the internal structure of a porous carbon fiber electrode. Lower void fractions increased peak power by 2.5% to 7.1% but resulted in pore clogging 3–5 times faster due to nonuniform deposition. It was found that staggered fiber arrangements maintained higher surface concentrations and 4.9% to 8.9% higher peak power compared to in-line fiber arrangements with the same void fraction while also displaying less dependence on fluid velocity due to efficient advection of reactants. An electrode with variable void fraction was designed to increase peak power by 7.5% but the pores clogged 23% faster compared to a similar electrode with a homogeneous void fraction.

1. Introduction

Power plants and industry generate an estimated 60 TWh of waste heat each year [1]. Roughly 66% of this energy is low-grade waste heat (temperature < 100 °C) meaning that it cannot efficiently be used by traditional thermal technologies for electrical power generation. Many researchers are investigating electrochemical and membrane-based systems for capturing this low-grade waste heat, including thermoelectrochemical cells, thermally regenerative electrochemical cycles, and thermally regenerative ammonia batteries (TRABs) [2]. However, all of these technologies currently show poor performance when considering factors such as power density, scalability, and cost, especially when comparing them to other renewable energy alternatives such as solar and wind energy [3]. Among these thermally-based electrochemical technologies, TRABs show the most promise for improvement and future competitiveness given that they have the highest power density and good efficiency relative to the Carnot cycle [2].

TRABs are a type of flow battery, which means that the electroactive components are stored in external tanks and pumped into an electrode stack where the electrochemical reaction occurs. However, they are charged by capturing thermal energy rather than consuming electrical power. All TRABs developed to date are hybrid flow batteries where both electrodes either grow in mass through metal deposition or are consumed due to metal depletion during the charge and discharge processes [4]. The electrodes are separated by an anion exchange membrane to prevent mixing of the electrolytes during operation while allowing anion transport through the membrane. An electric potential difference between two identical electrodes and electrolytes is created by adding a ligand, typically ammonia, to one electrolyte to form the anolyte. During discharge, the metal anode dissolves to create a

* Corresponding author.
E-mail address: matthew.rau@psu.edu (M.J. Rau).

https://doi.org/10.1016/j.electacta.2021.138527
0013-4686/

metal-ligand complex in the anolyte, and the aqueous metal in the catholyte is deposited onto the cathode. To use thermal energy to regenerate the battery, the ammonia is separated from the metal complex in the anolyte into a pure ammonia stream using low-grade waste heat in a process such as distillation. The ammonia can then be added into the spent catholyte to return the battery to a fully charged state [5]. Multiple iterations of TRABs have been investigated using cheap, abundant metals such as copper, nickel, and zinc, and have been able to obtain high power densities using zero-gap flow designs, nanoslurry, and maximizing the open circuit potential [6–8]. However, these chemistries have poor electrode reaction efficiencies and solubility of the active metals, resulting in poor cyclability of the battery [4,8–16]. A recent improvement of the TRAB was realized through the use of porous carbon electrodes and silver as the active metal (referred to as the Ag-TRAB), which resulted in electrode reaction efficiencies of over 95% [3]. This Ag-TRAB was cycled over 100 times with no appreciable decay in performance.

While TRABs have higher power densities than other electrochemical systems that capture low grade waste heat, TRABs have lower power densities than electrically-recharged flow batteries that use metals and complexes such as vanadium and zinc-bromine [17]. One potential method to improve power density of TRABS is by using porous electrodes, which have become ubiquitous in flow battery research because of their cyclability [3,18,19], high active surface area, and lower internal resistances compared to batteries with flow over the electrodes [20]. Critical to this approach is ensuring effective use of the electrode volume and avoiding dead zones in the electrolyte flow path [21–25]. Maximizing the use of the electrode volume prevents concentration polarization and provides better load tolerance [26]. Flow fields that distribute the electrolyte evenly throughout the volume of the electrodes will produce more uniform electrode utilization [22,26,27], but in order to properly design new flow fields it is important to understand what governs mass transfer within the porous electrodes. Understanding this is especially critical in TRABs as the metal deposition can clog pores and create preferential flow paths, limiting the performance of the battery. Even in fully aqueous flow batteries the type of porous material, its specific surface area, and the orientation of the fibers impacted rates of mass transfer of the system and were important determining factors in the length needed for single-pass conversion of the reactants [28,29]. Similarly, improved mass transfer due to increased fluid velocity in porous redox flow battery electrodes resulted in lower overpotentials and increased overall battery power output [30–32]. Researchers have improved battery performance by creating custom electrodes to enhance mass transfer by manipulating the fiber alignment and electrode microstructure [33–35]. Their electrodes increased the mass transfer coefficient by 50% compared to commercially available felts at a constant Reynolds number and increased the power density of the battery by 20%.

To understand how electrode fiber arrangement and metal deposition influences advective transport in TRAB electrodes as well as to improve their design and power output, we developed a 2D numerical model of the Ag-TRAB cathode. The electrode characteristics were simulated using two fiber arrangements and three different void fractions to study the relationship between fluid flow rate, porous electrode structure, battery power output, and electrodeposition uniformity at a constant electrolyte inlet concentration. Cylinders were oriented in a cross-flow arrangement to provide a two-dimensional analogue for the internal fiber structure of the carbon electrode. The impacts of fiber arrangement, void fraction, and flow rate on the peak power, deposition uniformity, and clogging of the electrode are demonstrated and used to guide how the electrode structure can be modified to extend battery discharge cycles.

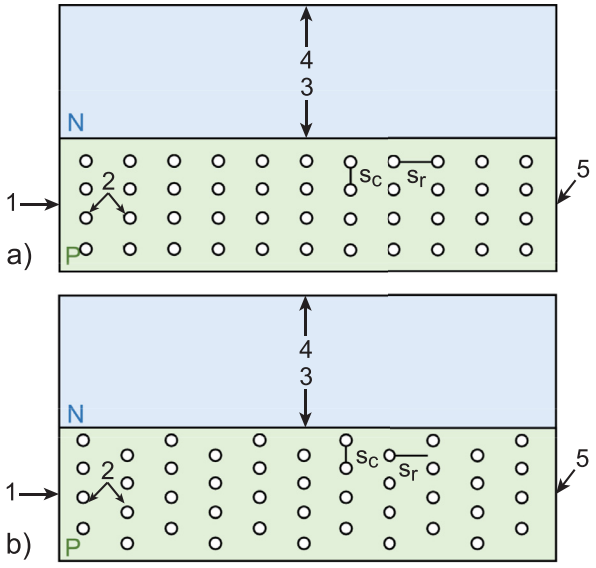

Fig. 1. Schematic of (a) in-line and (b) staggered fiber arrangements. Domains are: N – negative channel (blue) and P – positive channel (green). Boundaries are: 1 – positive electrolyte inlet, 2 – positive electrode surface, 3 – ion exchange membrane, 4 – negative electrode, and 5 – positive electrolyte outlet. Dimensions are not to scale (For interpretation of the references to color in this figure legend, the reader is referred to the web version of this article.).

2. Numerical methods

2.1. Computational domain and fiber arrangements

We developed the Ag-TRAB flow model using COMSOL Multiphysics [36]. The computational domain consisted of two channels, a positive electrolyte channel containing the fiber array (channel P), and a negative electrolyte channel to complete the electric circuit (channel N) (**Fig. 1**). The positive channel contained flowing electrolyte and concentration-dependent Butler-Volmer kinetics with tracking of the Ag^+, NH_4^+, and NO_3^- ions within the electrolyte. The positive electrolyte was silver nitrate with ammonium nitrate as the background electrolyte to simulate the solutions used in Ag-TRABs [3]. The electrochemical reaction present at the surface of the positive electrode fibers was [37]:

$$Ag^+(aq) + e^- \rightarrow Ag(s);\ E^0 = 0.7996\ V, \quad (1)$$

where E^0 is the standard electrode potential under standard conditions of 25 °C and 0.1013 MPa. The negative channel contained a stagnant electrolyte with a linear electrochemical ohmic drop and no overpotential at the electrode surface. The negative electrode reaction was a generic oxidation reaction that occurred at the channel wall (**Fig. 1**). The purpose of the negative electrode was to complete the circuit and, as a result, no reaction was specified for the negative side of the flow cell. We set the equilibrium potential of the negative electrode reaction to 0.35 V, as this is approximately the standard potential for the anode in the Ag-TRAB [3]. We separated the two channels with an infinitely-thin ion exchange membrane boundary plane to allow passage of NO_3^-(aq). We set the concentration of charge carriers in the membrane to 10 mol L^{-1} and the conductivity of the negative channel to 100 S cm^{-1}, values that were intentionally high to ensure that the resistance of the negative chamber was a negligible factor in cell performance. The high conductivity of the negative electrolyte and membrane, as well as the membrane being infinitely-thin, resulted in the peak power density being much larger than what has been reported previously for the Ag-TRAB. Thus, while the values for peak power output reported in this study are higher than what can be

obtained experimentally, the trends in peak power density that result from varying fiber arrangement, void fraction, and fluid velocity can still be applied to improve battery performance.

The cathode was designed to contain cylindrical fibers in varying arrangements using a script in COMSOL Livelink for MATLAB [36] to ensure consistent and precise spacing of all rows and columns. Each fiber had a diameter of 10 μm as this is similar to the average fiber diameter for many different porous carbon materials [38]. In all simulations, there were four fibers per column, where the vertical spacing between each fiber surface, S_r, was 15 μm. We varied the horizontal spacing between each column of fibers, S_c, to target three different void fractions: 80, 85, and 90%, as these were similar to different porous carbon materials [38]. The void fraction was defined as:

$$\varepsilon = \frac{V_{ch} - \sum_1^{n_{fib}} V_{fib}}{V_{ch}}, \tag{2}$$

where V_{ch} was the volume of the channel, V_{fib} was the volume of one fiber, and n_{fib} was the total number of fibers for that void fraction.

The fibers were organized in-line and staggered arrangements. In the in-line arrangement, we aligned the center of each fiber in each row (**Fig. 1a**). In the staggered arrangement, we vertically positioned the center of each fiber between the fibers in the previous column (**Fig. 1b**). We chose the flow channel height to be similar to experimental implementations of the Ag-TRAB [3]. The height of both negative and positive channels was 100 μm for the in-line arrangement and 107.5 μm for the staggered arrangement, which needed to be slightly taller to compensate for the adjusted position of the fibers. The minimum spacing between the fibers and the wall was 7.5 μm for the in-line arrangement and 5 μm for the staggered arrangement. The length of the channels was approximately 1000 μm, which we adjusted slightly with the different electrode geometries so that the spacing behind the last column of fibers was constant at 10 μm throughout all simulations. The out-of-plane thickness was constant at exactly 1000 μm.

2.2. Governing equations

The inlet fluid velocities ranged from 0.1 to 4 m s^{-1}, which resulted in Reynolds numbers from 1.5 to 60 based on the definition for flow around a cylinder [39], defined as

$$Re = \frac{\rho \bar{u} d_{fib}}{\mu}, \tag{3}$$

where ρ is the fluid density, $\bar{u}$ the average fluid velocity, d_{fib} the fiber diameter, and μ the dynamic fluid viscosity. The resulting Reynolds number range spanned three typical wake regimes for cylinders in cross-flow: a laminar wake with unseparated flow, $Re < 5$; a laminar wake with a fixed pair of attached vortices, $5 < Re < 40$; and the formation of a laminar vortex street, $40 < Re < 150$ [39]. The transition to a turbulent vortex street begins at $Re \approx 150$; thus, we modeled the flow assuming laminar conditions with no transition to turbulence.

The incompressible Navier-Stokes and continuity equations governed the fluid flow,

$$\rho \frac{\partial \vec{u}}{\partial t} + \rho(\vec{u} \cdot \nabla)\vec{u} = -\vec{\nabla} p + \mu \vec{\nabla}^2 \vec{u}, \tag{4}$$

$$\nabla \cdot \vec{u} = 0, \tag{5}$$

where p was the pressure of the fluid, $\vec{u}$ is the velocity vector, and t is time [40]. We imposed a no-slip boundary condition at all walls in the positive electrolyte channel. While the simulations of interest were time-dependent, we initialized the flow field in the first step of the time-dependent simulations using a steady-state solution of just the fluid flow in the absence of electrochemical transport (*i.e.* the solution to just Eqs. (4) and (5)). This initialization allowed for easier convergence of the first time-step in the time-dependent simulations and reduced total computational time. Fluid parameters used in the simulations are listed in **Table 1**.

Table 1
Fluid parameters used in all simulations.

Description	Variable	Value	Units
Fluid pressure	p	0.1013	MPa
Temperature	T	298.15	K
Fluid density	ρ	1379	kg m^{-3}
Fluid dynamic viscosity	μ	0.00092[a]	Pa s
Fluid normal inflow velocity	u	0.1, 0.5, 1, 2, 4	m s^{-1}
Fluid outlet pressure	p_{out}	0	atm

[a] Fitted parameter, see Supplementary Information, Section 2.

The positive channel was governed by the electroneutrality condition,

$$\sum z_i c_i = 0, \tag{6}$$

where z was the charge of each ion, and c_i was the bulk molar concentration of each species. In all simulations, NH_4^+(aq) was used as the conserved ion in the solution, with the total amount in the channel constant.

The flux and concentration change of all species in the positive channel were governed by the conservation of mass and convection-diffusion equations [41],

$$\frac{\partial c_i}{\partial t} + \vec{\nabla} \cdot \vec{N}_i = 0, \tag{7}$$

$$\vec{N}_i = -D_i \vec{\nabla} c_i - \frac{z_i F}{RT} D_i c_i \vec{\nabla} \phi_e + \vec{u} c_i, \tag{8}$$

where $\vec{N}_i$ was the flux and D_i was the diffusion coefficient of an individual species, F was Faraday's constant, R was the molar gas constant, T was the thermodynamic temperature of the fluid, and ϕ_e was the potential of the electrolyte. The combination of Eqs. (6) and (8) and the conservation of the ammonium ion concentration allows modeling of the electrolyte potential in the simulation domain. We calculated the equilibrium potential using the Nernst equation [41],

$$E_{eq} = E^0 + \frac{RT}{nF} \ln\left(a_{Ag^+(aq)}\right), \tag{9}$$

where n is the number of electrons transferred, as it would be specifically written for the electrochemical reaction in Eq. (1) where $a_{Ag+(aq)}$ was the activity of Ag^+(aq). The Ag^+(aq) activity was calculated to be 0.81 based on the activity coefficient being 0.2605 at ionic strength of 7 M [42] and the molality of Ag^+(aq) being 3.12 mol kg^{-1}. The Ag^+(aq) activity was assumed to be constant for all simulations ran. The properties of the positive electrolyte are listed in **Table 2**.

The local current density, j_{loc}, was modeled using the concentration-dependent version of the Butler-Volmer equation [43],

$$j_{loc} = j_0 \left[\frac{c_a^s}{c_a^o} \exp\left(\frac{\alpha_a F \eta}{RT}\right) - \frac{c_c^s}{c_c^o} \exp\left(-\frac{\alpha_c F \eta}{RT}\right) \right], \tag{10}$$

where j_0 was the exchange current density, $c_a{}^s$ was the surface molar concentration of the oxidized species, $c_a{}^o$ was the bulk molar concentration of the oxidized species, α_a was the anodic transfer coefficient, $c_c{}^s$ was the surface molar concentration of the reduced species, $c_c{}^o$ was the bulk molar concentration of the oxidized species, and α_c was the cathodic transfer coefficient. For all simulations, we assumed the concentration of the anodic species

Table 2
Positive electrolyte properties used in all simulations.

Description	Variable	Value	Units
Ag^+ Diffusion coefficient	D_{Ag+}	5.07×10^{-10}[a]	$m^2\ s^{-1}$
NH_4^- Diffusion coefficient	$D_{NH_4^+}$	6.33×10^{-10}[a]	$m^2\ s^{-1}$
NO_3^+ Diffusion coefficient	$D_{NO_3^-}$	5.69×10^{-10}[a]	$m^2\ s^{-1}$
Ag^+ Charge	z_{Ag+}	1	–
NH_4^+ Charge	$z_{NH_4^+}$	1	–
NO_3^- Charge	$z_{NO_3^-}$	−1	–
Ag^+ Bulk/inlet concentration	$c_{Ag+,i}$	2	mol L^{-1}
NH_4^+ Bulk/inlet concentration	$c_{NH_4^+,i}$	5	mol L^{-1}
NO_3^- Bulk/inlet concentration	$c_{NO_3^-,i}$	7	mol L^{-1}

[a] Estimated parameter, see Supplementary Information, Section 1.

Table 3
Electrode kinetic and thermodynamic parameters used in all simulations.

Description	Variable	Value	Units
Positive electrode equilibrium potential	$E_{eq,+}$	0.795	V
Exchange current density	j_0	18.35[a]	A m^{-2}
Anodic transfer coefficient	α_a	0.5	–
Cathodic transfer coefficient	α_c	0.35[a]	–
Number of participating electrons	n	1	–
Ag^+ stoichiometric coefficient	ν_{Ag+}	−1	–
Negative electrode equilibrium potential	$E_{eq,-}$	0.35	V
Negative electrode overpotential	η_-	0	V

[a] Estimated parameter, see Supplementary Information, Section 1.

to be negligible due to the electrode polarization, thus the anodic concentration ratio was set to a value of one and the anodic transfer coefficient to a value of 0.5. For all simulations, $c_c{}^s$ was the Ag^+(aq) molar surface concentration ($c^s{}_{Ag+(aq)}$), and $c_c{}^o$ was the inlet/bulk Ag^+(aq) molar concentration, a constant value of 2 mol L^{-1}. The overpotential, η, was defined as

$$\eta = \phi_s - \phi_{e,s} - E_{eq}, \tag{11}$$

where $\phi_{e,s}$ is the potential of the electrolyte in the mesh cell adjacent to the electrode surface, and ϕ_s was the potential of the electrode surface [44]. The kinetic and thermodynamic values used in all simulations are listed in **Table 3**.

The boundary condition describing consumption of the Ag^+(aq) at the positive electrode surface, (boundary 4 in **Fig. 1**) was

$$-\vec{N}_{Ag^+(aq),s} \cdot \vec{n} = -\frac{j_{loc}}{F}\ . \tag{12}$$

Eq. (12) does not apply to the ammonium and nitrate ions in the electrolyte as they were not involved in the electrochemical reaction. At the positive electrolyte inlet, (boundary 3 in **Fig. 1**), we defined a constant fluid velocity and used Danckwerts boundary condition for concentration,

$$\vec{n} \cdot \left(\vec{N}_i + \vec{u}c_i\right) = \vec{n} \cdot \left(\vec{u}c_i^o\right), \tag{13}$$

meaning that the rate of change of the concentration was zero across the boundary [45]. We applied the Danckwerts boundary condition to avoid issues such as a singularity that could result from the high reaction rate at the electrode surface near the inlet boundary of the positive electrolyte channel. At the outlet of the positive channel (boundary 7 in **Fig. 1**), we set the pressure of the fluid, the flux of ions, and the flux of electrons to zero. The membrane potential was equivalent to the potential of the electrolyte in the negative channel to ensure a continuous potential across the boundary.

To create power curves, the anode was maintained as ground and the surfaces of the fibers in the positive channel were subjected to a constant external electric potential that was swept from the value of the open circuit potential (0.45 V) to negative external potentials. Each external potential was held constant for one second of simulation time to model the current production and electrode thickness change over that time duration. After one second, we reset the fiber boundaries back to their original size and shape and stepped to the next external potential value. The current output of the cell was calculated for each potential step, j_{cell}, using a line integral summed over all fibers,

$$j_{cell} = t_{oop} \sum_{k=1}^{n_{fib}} \int_{L_k} j_{loc,k}\ ds_k, \tag{14}$$

where t_{oop} was the out-of-plane thickness of the simulation, L_k was the circumference of each individual fiber in the model, and ds_k was the arc length for integration. The power density was calculated as

$$P = \frac{j_{cell}\ E_{cell}}{SA}, \tag{15}$$

where the cell potential, E_{cell}, was obtained by taking the average positive electrode potential and subtracting the potential of the negative electrode (a constant value for all simulations). We normalized the power output to the active electrode surface area, SA, to allow for direct comparison between each void fraction and electrode arrangement.

The fiber thickness change was calculated from the surface concentration of Ag(s), $c^s{}_{Ag(s)}$, which was governed by

$$\frac{dc^s_{Ag_{(s)}}}{dt} = \frac{\nu j_{loc}}{nF}, \tag{16}$$

where ν was the reaction stoichiometry. Deposition was simulated as a distributed layer on all fiber surfaces as opposed to the formation of silver particles but allowed deposition to be nonuniform around the circumference of each fiber based on the local current distribution. The fiber thickness change was calculated using

$$\Delta t_{fib} = \frac{M_{Ag}}{\rho_{Ag}} \int_0^1 \frac{dc^s_{Ag_{(s)}}}{dt}, \tag{17}$$

where Δt_{fib} was the fiber thickness change over the one second simulation time, M_{Ag} was the molar mass of silver, and ρ_{Ag} was the density of metallic silver. Parameters for quantifying power and thickness change are listed in **Table 4**. We extracted the values for the fiber thickness change from four different locations on each fiber: the front, back, top, and bottom.

Table 4
Parameters that were held constant for quantifying power output and thickness change.

Description	Variable	Value	Units
Out-of-plane thickness	t_{oop}	0.001	m
Ag Density	ρ_{Ag}	10,500	kg m^{-3}
Ag Molar mass	MM_{Ag}	0.107868	kg mol^{-1}

2.3. Computational mesh

A mesh independence study was completed to determine overall mesh fineness and whether the mesh elements should be more concentrated in the fluid bulk or at the boundaries of the system. The case used had 80% void fraction, the in-line arrangement, and Re = 15 (fluid velocity = 1 m s^{-1}) for this mesh study. Increasing the total number of mesh elements from 120,000 to 185,000 by refinement of the element size resulted in less than a 0.1% change in the peak power output. This trend was consistent at all current densities studied. We also found that boundary layer meshes with four elements represented the best compromise between properly resolving the small concentration gradients at the electrode surfaces and computational cost. The change in electrode thickness, which is directly proportional to Ag^+(aq) surface concentration, varied by less than 0.5% between the coarsest and finest boundary

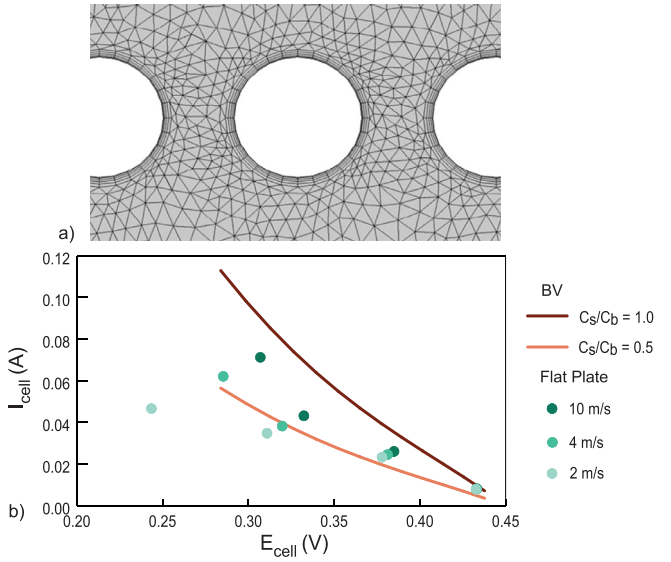

Fig. 2. (a) Finalized mesh around three in-line fibers in the computational domain. (b) Comparison of the Butler-Volmer equation (with IR correction) to COMSOL results for a channel geometry using the same simulation parameters as the rest of the study.

meshes we considered. Our final mesh contained 33,436 quadrilateral boundary elements and 119,628 triangular elements.

A complete list of mesh parameters can be found in the Supplementary Information, Section 3. **Fig. 2a** shows the finalized mesh around three in-line fibers. The model was solved using a multifrontal massively parallel sparse (MUMPS) direct solver for all simulations.

2.4. Model verification

To verify the output of our model, we compared the simulated current output for flow over a flat plate electrode to the current output as modeled by just the Butler-Volmer equation. The flat plate simulations were identical to the fiber-arrangement models in the kinetic and electrolyte parameters, but the simplified geometry avoided any influence from the flow field produced by the fibers. Since the COMSOL overpotential accounts for the IR drop of the electrolyte (see Eq. (11)), we used the cell potential for comparison. The cell potential was defined as

$$E_{cell} = E_{OCP} - \eta - I_{cell}R_{elec}, \tag{19}$$

where E_{OCP} was the open circuit potential, and R_{elec} was the resistance of the electrolyte.

The Butler-Volmer curves shown in **Fig. 2b** (labeled BV) assume a constant electrode surface concentration, whereas our flow cell simulations allow the surface concentration to vary locally based on flow and mass transfer effects. Plotted for comparison are theoretical concentration ratios of one (BV $c_s/c_b = 1$) and 0.5 (BV $c_s/c_b = 0.5$). At low fluid velocities, our simulations resulted in much lower current output compared to the Butler-Volmer equation (where BV $c_s/c_b = 1$), as expected as the concentration boundary layer that developed in the flow channel limited the surface concentration at the electrode surface. These results were closer to the Butler-Volmer equation with a concentration ratio of 0.5. As the simulated fluid velocity increased, the thinner boundary layer and higher mass transfer resulted in higher surface concentrations and the results approached the theoretical limit provided by the Butler-Volmer equation (**Fig. 2b**). Thus, we concluded that our model was appropriately capturing the concentration-dependent variations in power output caused by the flow field of our geometry.

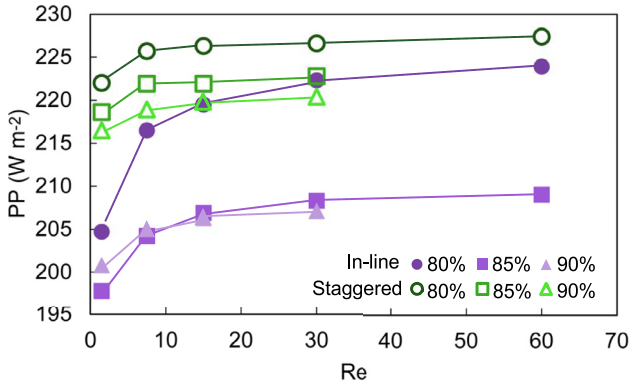

Fig. 3. Peak power density for both fiber arrangements and all three void fractions as a function of fiber Reynolds number. Power densities are normalized to total active electrode surface area.

3. Results and discussion

3.1. Peak power density

The influence of the Reynolds number on the power output of each electrode arrangement is demonstrated by extracting the peak power density (*PP*) from each simulated power curve (**Fig. 3**). For the staggered arrangements, the peak power densities decreased inversely with the void fraction, with the 80% void fraction producing the peak power density of 227 W m^{-2} and the 90% void fraction the lowest 220 W m^{-2}. These porosities produced an overall difference of ~2.5 W m^{-2} between the 90% and 85% void fractions and a ~4 W m^{-2} difference between the 85% and 80% void fractions across all Reynolds numbers. The peak power density of the staggered cases was only minimally sensitive to the Reynolds number, increasing by ~1.5% from a *Re* of 1.5 to 7.5, and only by ~0.75% from a *Re* of 7.5 to 60 across all void fractions.

The in-line results also produced the highest power densities with the lowest porosities, with the 80% void fraction maintained the highest peak power density at all Reynolds numbers for the in-line arrangements, with the 85% void fraction having the next highest peak power density for Reynolds numbers greater than or equal to 15. Below a Reynolds number of 15, the 90% void fraction had a higher peak power density than the 85% void fraction. The peak power densities of the 90% void fraction were also relatively insensitive to the flow velocities with only a ~1% increase in power for Reynolds numbers above 7.5. In contrast, the power density of the 80% and 85% void fractions showed a greater dependence on flow velocity. The peak power density of the 85% void fraction increased by 2.5% over the same Reynolds number range, an increase two and a half times higher than that of all the staggered cases and the in-line case with 90% void fraction. The peak power density of the 80% void fraction increased by roughly 9%, which was the strongest dependence on Reynolds number of all electrode geometries. This increase corresponded to 19.2 W m^{-2}, which was more than twice the gains of the other in-line arrangements and three times the gains from all void fractions in the staggered arrangement over all Reynolds numbers studied.

3.2. Deposition uniformity

Higher void fractions and the staggered arrangement resulted in more uniform deposition along the channel length (**Fig. 4a**). For the in-line arrangement, the difference between the minimum and maximum deposition was 5%, 2.6%, and 1.1% for void fractions of 80%, 85%, and 90%, respectively. For the staggered arrangement, the difference between the minimum and maximum deposition was

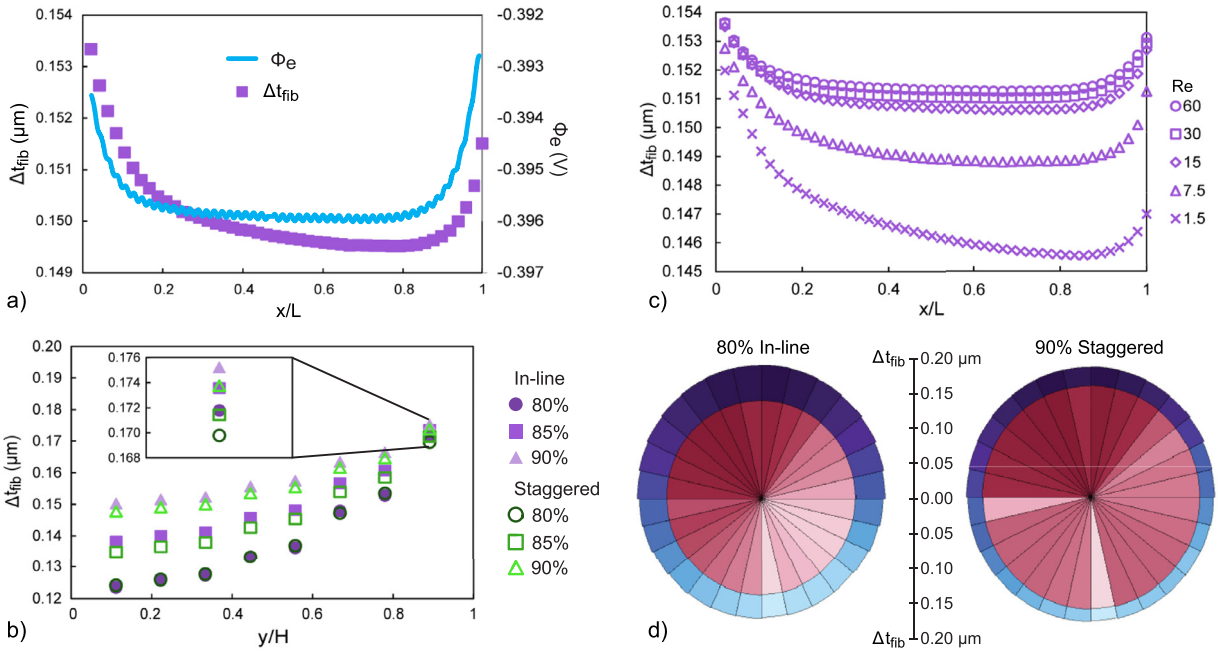

Fig. 4. (a) Fiber thickness change and IR drop at y/H = 0.5 along the length of the channel for the 85% in-line case. (b) Fiber thickness change across the height of the channel for each arrangement and void fraction averaged over all columns in the channel and all *Re* (inset is a magnification of the data for the fibers closest to the membrane). (c) Fiber thickness change along the flow path of the electrolyte for the in-line case with 85% void fraction at different *Re*. (d) Rose plot of fiber thickness change around the circumference of a cylinder in the first column and top (outer, blue) or bottom (inner, pink) row. Lighter shades correspond to less thickness change and darker shades correspond to more. All data for this figure was taken after simulating 1 s of deposition at a constant external potential of 0.1 V (For interpretation of the references to color in this figure legend, the reader is referred to the web version of this article.).

3%, 1.7%, and 0.5% for void fractions of 80%, 85%, and 90%, respectively. The lower void fractions had less uniform deposition largely due to electric field effects. Equipotential contours are known to converge at the ends of planar electrodes [41], which for this study resulted in the electrolyte potential being stronger and the deposition being more nonuniform at the channel entrance and entrance and exit (**Fig. 4a**). By comparing the deposition profile along the channel length to the IR drop along the center of the channel for the in-line case with 85% void fraction (**Fig. 4a**), we can see that the deposition pattern largely followed the IR drop. Deposition in the middle of the channel ($0.2 < x/L < 0.8$) generally decreased along the flow length due to poor advective transport, which was more substantial for electrodes with higher surface area. However, due to the short length of this channel, this effect was minimal. The maximum total consumption of Ag^{+}(aq) was only 3% for all cases studied, therefore the bulk concentration was constant for the entire length of the channel.

Higher void fractions also resulted in more uniform deposition from the bottom to the top of the channel for all fluid velocities studied, but there was little difference in uniformity between the in-line and staggered arrangements in this direction (**Figs. 4b**, **4d**). For the in-line arrangement, the difference between the minimum and maximum deposition was 25%, 19%, and 13% for void fractions of 80%, 85%, and 90%, respectively. For the staggered arrangement, the difference between the minimum and maximum deposition was 25%, 20%, and 14% for void fractions of 80%, 85%, and 90%, respectively.

Higher fluid velocities produced more uniform deposition along the length of the flow channel (**Fig. 4c**). The difference between the maximum and minimum deposition was 4.7% and 1.7% for the lowest and highest Reynolds numbers, respectively. Though only results for the in-line arrangement with 85% void fraction are plotted, this trend was consistent across all electrode arrangements and void fractions. In general, the relationship between the thickness change and the Reynolds number resembled the trend observed for peak power density, where most cases showed little change above a *Re* of 15.

The above deposition comparison was made at an external electric potential of 0.1 V. At this potential, the current density, in addition to the power density, was similar for all six electrode geometries (±9% for current density and ±5% for power), and below peak power for all six electrode geometries. Thus, this operating condition represented a better comparison for deposition thickness given that current density has the greatest impact on deposition thickness as per Eqs. (16) and (17). At peak power or higher power outputs, these non-uniformity trends would be further exacerbated with deposition becoming less uniform at higher power output.

3.3. Impact of electric field

The strong dependence of peak power density on void fraction can be explained largely by the electrolyte IR drop (ϕ_e in Eq. (11)) across the height of the channel (**Fig. 5a**). Lower void fractions led to higher electrolyte IR drop, with total values for the 80% void fractions being almost double that of the electrodes with 90% void fraction. The larger potential drop produced by the more densely packed electrode was consistent with the higher power output of the lower void fraction and was the main driver for higher power output. The difference in the total IR drop between the different void fractions of the staggered arrangements was roughly the same at ~15 mV, just as the change in power density was constant between the different void fractions for this arrangement (**Fig. 3**). In contrast, there was a ~20 mV difference between the in-line arrangement with the 80% and 85% void fraction. The smaller spacing between the fibers with 80% void fraction caused a stronger electric field between the top row and the membrane compared to the other void fractions, creating a larger IR drop across this top row of fibers (shown at a dimensionless height of 0.85 in **Fig. 5**). The higher IR drop of this top fiber row meant that more current passed through the electrolyte at this location. Since the deposition

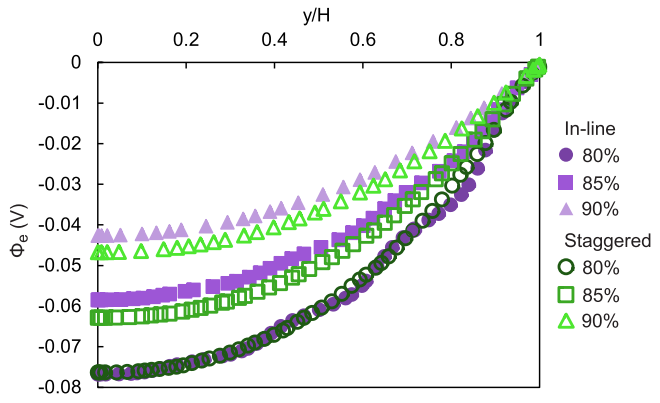

Fig. 5. Electrolyte IR drop across the dimensionless height of the channel at its midpoint for all six cases studied at a Reynolds number of 15, external electric potential of 0 V, and simulation time of 1 s. The location of the membrane is at $y/H = 1$.

thickness is directly related to the current, the deposition patterns across the channel height followed the potential drop of the electrolyte. This is evident by comparing the shape of the deposition thickness change (Fig. 4**b**) to the IR drop (Fig. 5) at each arrangement and void fraction.

3.4. Impact of advection

Of the six cases studied, the peak power density and deposition uniformity had the strongest dependence on fluid velocity for the in-line arrangement with 80% and 85% void fraction. Fluid streamtraces show that vortex formation near the fibers was highly dependent on the arrangement and spacing of the fibers (Fig. 6). The streamtraces for the staggered arrangement with 80% void fraction (Fig. 6) indicate minimal flow separation occurred at $Re = 15$. For a single cylinder in an infinite fluid at this Reynolds number, we would expect a fixed pair of vortices to form in the cylinder wake. These vortices were suppressed due to the close proximity of the surrounding fibers in the staggered arrangement at this 80% void fraction [46]. Even at higher Reynolds numbers (up to $Re = 60$), we did not observe flow separation for this electrode. Because of the minimal flow separation, the $Ag^+(aq)$ concentration around the fiber surfaces remained close to the bulk concentration for this electrode, a result that extended to all Reynolds numbers studied (Fig. 7). For the staggered arrangements with 85% and 90% void fractions (Fig. 6**c** and **e**), the fibers were spaced sufficiently to allow the development of two fixed vortices. There was increased mass transfer at the locations where boundary layer separation occurred, resulting in higher $Ag^+(aq)$ consumption at the outer edges of each vortex. Despite these differences in the flow fields, the average surface concentration of all fibers in the channel for the staggered void fractions was similar across all fluid velocities, indicating that void fraction had little impact on mass transfer losses for the staggered arrangement (Fig. 7). These high surface concentrations, in addition to the IR drop effects discussed above, explain the consistently higher power output of the staggered electrode arrangement than the in-line configuration.

The flow field around all fibers in the in-line arrangement showed two fixed vortices behind each fiber regardless of void fraction (Fig. 6**b, d**, and **f**), but the close spacing of the 80% and 85% void fractions did not allow for the full development of these vortices (Fig. 6**b**, and **d**). This vortex generation as a function of cylinder spacing was consistent with previous literature that found that there is a transition in vortex shape and size when the spacing

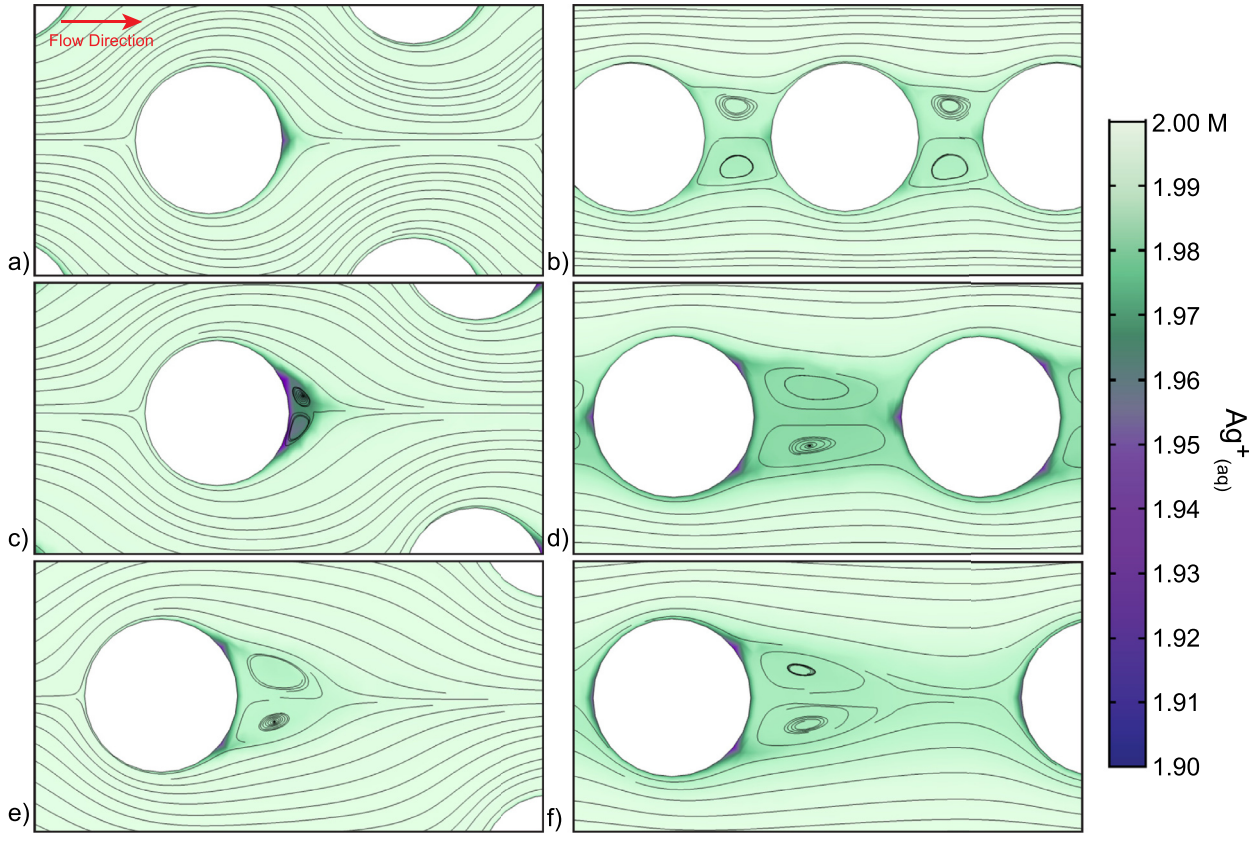

Fig. 6. Velocity streamtraces overlaid with contours of $Ag^+(aq)$ concentration for (a) 80% Staggered, (b) 80% In-line, (c) 85% Staggered, (d) 85% In-line, (e) 90% Staggered, and (f) 90% In-line. Concentration is presented in units of mol L^{-1}. Cases were at $Re = 15$ and an external electric potential of 0 V.

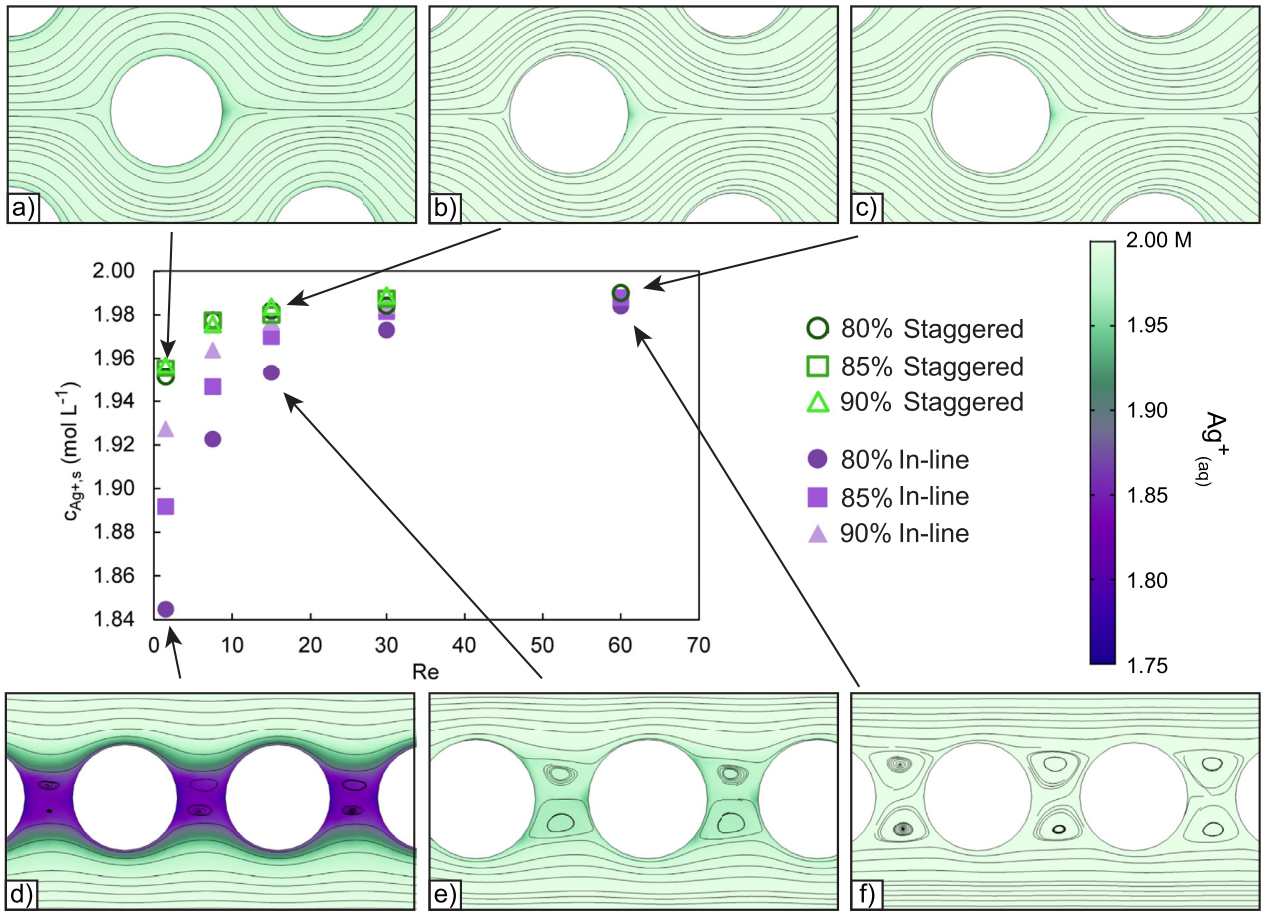

Fig. 7. Velocity streamtraces overlaid with contours of $Ag^+(aq)$ concentration for the 80% staggered case at (a) $Re = 1.5$, (b) $Re = 15$, (c) $Re = 60$, and 80% in-line case at (d) $Re = 1.5$, (e) $Re = 15$, (f) $Re = 60$. Concentration is presented in mol L^{-1}. Average surface concentration of $Ag^+(aq)$ for all cylinders in the channel across all Reynolds numbers studied. Data was taken at an external electric potential of 0 V and after 1 s of simulation time at the peak power density for each case.

between in-line cylinders exceeds one diameter [47]. For the 80% and 85% void fractions, these vortices occupied the majority of the gap between adjacent fibers, which allowed for less replenishment of $Ag^+(aq)$ in this space. The lack of replenishment was particularly evident at low Reynolds number for the 80% void fraction case (**Fig. 7d**). These regions of depleted electrolyte resulted in low average electrode surface concentrations, meaning high mass transfer losses for this case (**Fig. 7**). As the fluid velocity increased, the vortices between fibers grew in size and in their ability to transport $Ag^+(aq)$ from the bulk, which resulted in the largest increase in surface concentration for this electrode with increasing Reynolds number (**Fig. 7**). In contrast, the flow path of the electrolyte in all staggered arrangements was such that there was never significant localized depletion of $Ag^+(aq)$ near the surface of the electrode. This dependence of the local concentration on the flow field explains why the power density of the in-line arrangements with 80% and 85% void fraction electrodes were much more dependent on the fluid velocity than those of the other electrode arrangements (**Fig. 3**).

3.5. Plugging time and variable void fraction electrode

We estimated the average time that it would take for a row of fibers in our electrodes to plug (defined as the time at which two adjacent fibers touch) by extrapolating the growth velocities of the Ag(s) deposition at peak power output. Since deposition occurred nonuniformly throughout our electrodes, we used the highest, row-averaged growth velocity, which occurred for the fibers closest to the membrane. For the in-line arrangements, plugging will first occur between the front and rear points of the fibers in the top row. For the staggered arrangements, plugging will first occur between diagonally-adjacent fibers in the top two rows (see **Fig. 8c** inset and SI, Section 4 for more detail). While calculating electrode plugging in this way does not take the formation of Ag(s) nuclei into account [3], it does allow a comparison of plugging potential based on power output and electrode arrangement and void fraction. The staggered arrangements had greater spacing compared to in-line arrangements with the same void fractions and, thus had longer plugging times except for the electrodes with 90% void fraction (**Fig. 8b**). The staggered arrangements had higher local current densities, which resulted in higher deposition growth velocity than the in-line arrangements. At all void fractions, in-line arrangements suffered shorter plugging time because of the shorter fiber spacing. However, as the void fraction increased, the growth velocity of the staggered arrangement increases more than the larger spacing between fibers causing the difference in plugging times between the two arrangements to become smaller.

The variation of the plugging time of both arrangements with the Reynolds number was consistent with the relationship between the peak power density and the Reynolds number for that case. The in-line arrangement with 80% void fraction had the shortest plugging time as a result of the strong electric field present at the top row of the electrode, as discussed previously, and the small spacing between adjacent fibers. The 90% void fractions had plugging times that were more than three times that of the 80% void fractions, meaning that the electrodes with higher

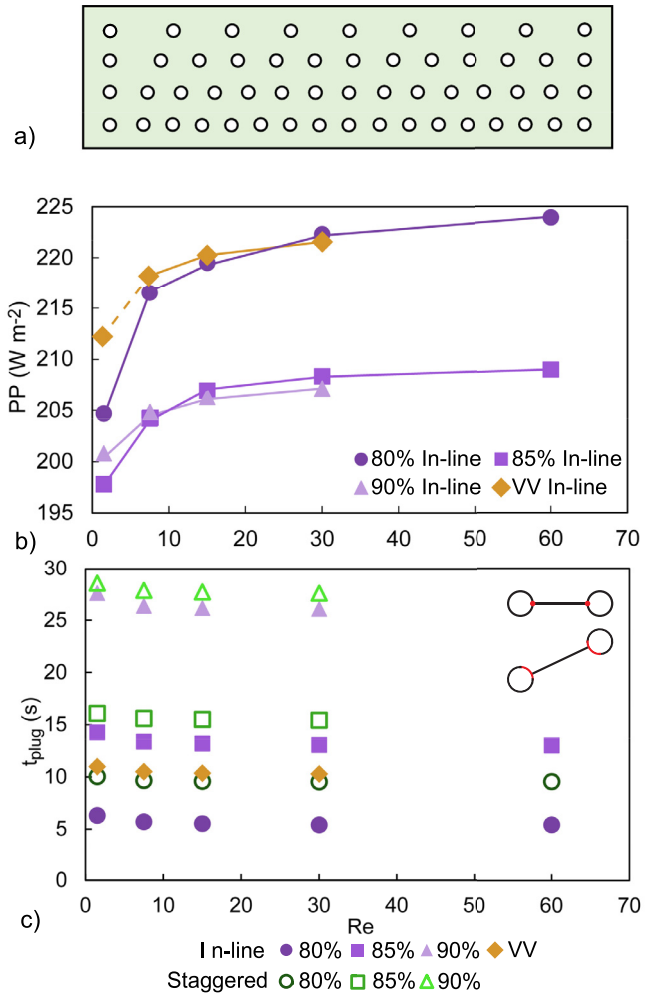

Fig. 8. (a) Schematic of the positive channel of the in-line arrangement with variable void fraction. Dimensions are not to scale. (b) Peak power density for all four in-line arrangements as a function of Reynolds number. (c) Extrapolated plugging time for the all arrangements studied. Data was taken from the front and back of the fibers in the top row for the 80, 85, and 90% void fractions, and bottom row for variable void fraction.

void fractions will avoid clogging and sustain their performance for longer periods of time, allowing for longer and more predictable performance during the charge and discharge cycle of the battery.

In an attempt to create an electrode that combined the advantages of the low void fractions (high power output) with high void fractions (more uniform surface concentration and longer plugging times), we created a modified in-line arrangement with variably-spaced fibers. In this design, the top row had an equivalent void fraction of 90%, followed by 86% for the second row, 83% for the third row, and 80% for the bottom row of fibers (**Fig. 8a**). This created an in-line electrode with a variable void fraction (termed VV) that had an average void fraction of 85%. Though unconventional, this electrode structure could be manufactured using recent advances in additive manufacturing [14,48]. The VV electrode had power output similar to that of the in-line arrangement with 80% void fraction (**Fig. 8b**) but with plugging times that were closer to that of the in-line arrangement with 85% void fraction (**Fig. 8c**).

The VV electrode produced higher peak power than the in-line arrangement with 85% void fraction because it sustained higher surface concentration of the Ag^{+}(aq), while also having similar electrolyte IR drop. The peak power of the VV electrode was 7.5% higher than the 85% void fraction. This was comparable to the increase in peak power previously obtained for a copper TRAB using an electrode with a gradient in void fraction along the flow direction compared to an electrode with a homogenous void fraction [14]. The VV electrode had an ~84% longer plugging time when compared to the in-line arrangement with 80% void fraction because the row with the highest electrode growth velocity (*i.e.* the row closest to the membrane) also had the largest column spacing (**Fig. 8a**). The above results from the VV electrode show that by modifying the fiber spacing to accommodate the expected non-uniform deposition, we can create electrodes that balance power output with longer discharge times. This or similar electrode designs also have the potential to mitigate the formation of preferential flow paths through the electrode due to non-uniform deposition during discharge, potentially leading to greater utilization of the entire electrode active surface area during battery operation.

3.6. Battery operation and battery implications

For the Ag-TRAB and other hybrid flow batteries that use porous electrodes, controlling electrodeposition throughout the electrode can be accomplished through the different means that have been previously discussed. During battery operation the electrolyte flow rate and operating current are critical parameters for the longevity of the electrode. For electrolyte flow rate, the trade-off between increased power output and increased pumping power requirement is well known, but for hybrid flow batteries there is an additional benefit of more uniform deposition. As the cell current is increased, the deposition will become less uniform throughout the electrode, meaning that the discharge or charge rate of the battery will significantly impact the performance and the efficiency of the electrode over each individual cycle. Operating the battery above peak power would be severely detrimental to electrode performance and would result in the poor utilization of the porous electrode volume.

While decreasing the electrode void fraction can be used to improve the power density of the battery, the gains are much smaller than the decrease in the time that it would take for the pores to clog. Therefore, it is recommended to use a high void fraction electrode for hybrid flow batteries to help extend the amount of time that the battery can discharge without significant decrease in performance from nonuniform electrodeposition. Since nonuniform growth occurs predominantly from electric field effects, the electrode microstructure could be redesigned to mitigate the negative effects of nonuniform electrodeposition. Pores in regions in the electrode that experience lower current densities (e.g. away from the membrane) will take longer to plug and therefore can be smaller without sacrificing the longevity of the electrode. In addition, these low current density regions provide a smaller share to the power output of the battery, meaning that their plugging would be less detrimental to the battery performance.

4. Conclusions

Electrodes with lower void fractions produced higher power density relative to their electroactive surface area due to increased ohmic contributions to the cell. The power output of the staggered arrangements was less sensitive to increasing fluid velocity compared to the in-line arrangements because of superior replenishment of Ag^{+}(aq) to the electrode surfaces due to delayed flow separation in the wake of the fibers. Across all cases, the deposition became more uniform along the length of the channel with increasing fluid velocity. The main cause of non-uniform deposition along both the length and height of the channel was the electric field. Electrodes with lower void fractions had higher IR drop through their thickness, resulting in less uniform deposition. Plugging times for our electrode geometries were estimated and found that electrodes with 90% void fractions can discharge for three to

five times longer than electrodes with 80% void fractions before significant plugging would occur. To balance longer plugging times with higher power outputs, an electrode with a variable void fraction was created. This electrode design had a similar electroactive surface area and plugging time compared to the in-line arrangement with 85% void fraction but sustained higher power output similar to that of electrodes with lower void fractions.

Declaration of Competing Interest

The authors declare that they have no known competing financial interests or personal relationships that could have appeared to influence the work reported in this paper.

Credit authorship contribution statement

Nicholas R. Cross: Conceptualization, Investigation, Methodology, Validation, Writing – original draft. **Derek M. Hall:** Methodology, Writing – review & editing, Supervision. **Serguei N. Lvov:** Methodology, Writing – review & editing. **Bruce E. Logan:** Writing – review & editing, Supervision. **Matthew J. Rau:** Conceptualization, Methodology, Writing – review & editing, Supervision, Funding acquisition.

Acknowledgments

This research was supported by the Pennsylvania State University Institutes of Energy and the Environment. Simulations were performed on the Pennsylvania State University's Institute for Computational and Data Sciences' Roar supercomputer.

Supplementary materials

Supplementary material associated with this article can be found, in the online version, at doi:10.1016/j.electacta.2021.138527.

References

[1] C. Haddad, C. Périlhon, A. Danlos, M.X. François, G. Descombes, Some efficient solutions to recover low and medium waste heat: competitiveness of the thermoacoustic technology, Energy Proced. 50 (2014) 1056–1069, doi:10.1016/j.egypro.2014.06.125.
[2] M. Rahimi, A.P. Straub, F. Zhang, X. Zhu, M. Elimelech, C.A. Gorski, B.E. Logan, Emerging electrochemical and membrane-based systems to convert low-grade heat to electricity, Energy Environ. Sci. 11 (2018) 276–285, doi:10.1039/c7ee03026f.
[3] M. Rahimi, T. Kim, C.A. Gorski, B.E. Logan, A thermally regenerative ammonia battery with carbon-silver electrodes for converting low-grade waste heat to electricity, J. Power Sources 373 (2018) 95–102, doi:10.1016/j.jpowsour.2017.10.089.
[4] F. Zhang, J. Liu, W. Yang, B.E. Logan, A thermally regenerative ammonia-based battery for efficient harvesting of low-grade thermal energy as electrical power, Energy Environ. Sci. 8 (2015) 343–349, doi:10.1039/c4ee02824d.
[5] F. Vicari, A. D'Angelo, Y. Kouko, A. Loffredi, A. Galia, O. Scialdone, On the regeneration of thermally regenerative ammonia batteries, J. Appl. Electrochem. 48 (2018) 1381–1388, doi:10.1007/s10800-018-1240-0.
[6] V.M. Palakkal, T. Nguyen, P. Nguyen, M. Chernova, J.E. Rubio, G. Venugopalan, M. Hatzell, X. Zhu, C.G. Arges, High power thermally regenerative ammonia-copper redox flow battery enabled by a zero gap cell design, low-resistant membranes, and electrode coatings, ACS Appl. Energy Mater. 3 (2020) 4787–4798, doi:10.1021/acsaem.0c00400.
[7] S. Maye, H.H. Girault, P. Peljo, Thermally regenerative copper nanoslurry flow batteries for heat-to-power conversion with low-grade thermal energy, Energy Environ. Sci. 13 (2020) 2191–2199, doi:10.1039/d0ee01590c.
[8] W. Wang, G. Shu, H. Tian, D. Huo, X. Zhu, A bimetallic thermally-regenerative ammonia-based flow battery for low-grade waste heat recovery, J. Power Sources 424 (2019) 184–192, doi:10.1016/j.jpowsour.2019.03.086.
[9] M. Rahimi, A. D'Angelo, C.A. Gorski, O. Scialdone, B.E. Logan, Electrical power production from low-grade waste heat using a thermally regenerative ethylenediamine battery, J. Power Sources 351 (2017) 45–50, doi:10.1016/j.jpowsour.2017.03.074.
[10] L. Zhang, Y. Li, X. Zhu, J. Li, Q. Fu, Q. Liao, Z. Wei, Copper foam electrodes for increased power generation in thermally regenerative ammonia-based batteries for low-grade waste heat recovery, Ind. Eng. Chem. Res. 58 (2019) 7408–7415, doi:10.1021/acs.iecr.9b00616.
[11] W. Wang, G. Shu, H. Tian, X. Zhu, Removals of Cu(II), Ni(II), Co(II) and Ag(I) from wastewater and electricity generation by bimetallic thermally regenerative electro-deposition batteries, Sep. Purif. Technol. 235 (2020) 116230, doi:10.1016/j.seppur.2019.116230.
[12] W. Wang, H. Tian, G. Shu, D. Huo, F. Zhang, X. Zhu, A bimetallic thermally regenerative ammonia-based battery for high power density and efficiently harvesting low-grade thermal energy, J. Mater. Chem. A 7 (2019) 5991–6000, doi:10.1039/c8ta10257k.
[13] Y. Shi, L. Zhang, J. Li, Q. Fu, X. Zhu, Q. Liao, Cu /Ni composite electrodes for increased anodic coulombic EF FI ciency and electrode operation time in a thermally regenerative ammonia- based battery for converting low-grade waste heat into electricity, Renew. Energy 159 (2020) 162–171, doi:10.1016/j.renene.2020.05.147.
[14] Y. Shi, L. Zhang, J. Li, Q. Fu, X. Zhu, Q. Liao, Y. Zhang, 3-D printed gradient porous composite electrodes improve anodic current distribution and performance in thermally regenerative flow battery for low-grade waste heat recovery, J. Power Sources 473 (2020) 228525, doi:10.1016/j.jpowsour.2020.228525.
[15] W. Wang, S. Yang, D. Huo, H. Tian, S. Li, X. Zhu, G. Shu, Understanding the reaction mechanism and self-discharge of a bimetallic thermally-regenerative ammonia battery, Electrochim. Acta. 370 (2021) 137724, doi:10.1016/j.electacta.2021.137724.
[16] Y. Zhang, L. Zhang, J. Li, X. Zhu, Q. Fu, Q. Liao, Y. Shi, Performance of a thermally regenerative ammonia-based flow battery with 3D porous electrodes: effect of reactor and electrode design, Electrochim. Acta 331 (2020) 135442, doi:10.1016/j.electacta.2019.135442.
[17] A.Z. Weber, M.M. Mench, J.P. Meyers, P.N. Ross, J.T. Gostick, Q. Liu, Redox flow batteries: a review, J. Appl. Electrochem. 41 (2011) 1137–1164, doi:10.1007/s10800-011-0348-2.
[18] J.F. Parker, C.N. Chervin, I.R. Pala, M. Machler, M.F. Burz, J.W. Long, D.R. Rolison, Rechargeable nickel-3D zinc batteries: an energy-dense, safer alternative to lithium-ion, Science (80-.). 418 (2017) 415–418. 10.1126/science.aak9991.
[19] J.F. Parker, C.N. Chervin, E.S. Nelson, D.R. Rolison, J.W. Long, Wiring zinc in three dimensions re-writes battery performance - dendrite-free cycling, Energy Environ. Sci. 7 (2014) 1117–1124, doi:10.1039/c3ee43754j.
[20] X. Ke, J.M. Prahl, I.J.D. Alexander, J.S. Wainright, T.A. Zawodzinski, R.F. Savinell, Rechargeable redox flow batteries: flow fields, stacks and design considerations, Chem. Soc. Rev. 47 (2018) 8721–8743, doi:10.1039/c8cs00072g.
[21] C.R. Dennison, E. Agar, B. Akuzum, E.C. Kumbur, Enhancing mass transport in redox flow batteries by tailoring flow field and electrode design, J. Electrochem. Soc. 163 (2016) A5163–A5169, doi:10.1149/2.0231601jes.
[22] N. Gurieff, C.Y. Cheung, V. Timchenko, C. Menictas, Performance enhancing stack geometry concepts for redox flow battery systems with flow through electrodes, J. Energy Storage 22 (2019) 219–227, doi:10.1016/j.est.2019.02.014.
[23] S. Kumar, S. Jayanti, Effect of flow field on the performance of an all-vanadium redox flow battery, J. Power Sources 307 (2016) 782–787, doi:10.1016/j.jpowsour.2016.01.048.
[24] M. Wu, T. Zhao, R. Zhang, H. Jiang, L. Wei, A zinc–bromine flow battery with improved design of cell structure and electrodes, Energy Technol. 6 (2018) 333–339, doi:10.1002/ente.201700481.
[25] I. Mayrhuber, C.R. Dennison, V. Kalra, E.C. Kumbur, Laser-perforated carbon paper electrodes for improved mass-transport in high power density vanadium redox flow batteries, J. Power Sources 260 (2014) 251–258, doi:10.1016/j.jpowsour.2014.03.007.
[26] J. Houser, A. Pezeshki, J.T. Clement, D. Aaron, M.M. Mench, Architecture for improved mass transport and system performance in redox flow batteries, J. Power Sources 351 (2017) 96–105, doi:10.1016/j.jpowsour.2017.03.083.
[27] B. Akuzum, Y.C. Alparslan, N.C. Robinson, E. Agar, E.C. Kumbur, Obstructed flow field designs for improved performance in vanadium redox flow batteries, J. Appl. Electrochem. 49 (2019) 551–561, doi:10.1007/s10800-019-01306-1.
[28] M.J. Kim, Y. Seo, M.A. Cruz, B.J. Wiley, Metal nanowire felt as a flow-through electrode for high-productivity electrochemistry, ACS Nano 13 (2019) 6998–7009, doi:10.1021/acsnano.9b02058.
[29] D. Schmal, J. Van Erkel, P.J. Van Duin, Mass transfer at carbon fibre electrodes, J. Appl. Electrochem. 16 (1986) 422–430.
[30] G. Qiu, C.R. Dennison, K.W. Knehr, E.C. Kumbur, Y. Sun, Pore-scale analysis of effects of electrode morphology and electrolyte flow conditions on performance of vanadium redox flow batteries, J. Power Sources 219 (2012) 223–234, doi:10.1016/j.jpowsour.2012.07.042.
[31] D. Zhang, A. Forner-Cuenca, O.O. Taiwo, V. Yufit, F.R. Brushett, N.P. Brandon, S. Gu, Q. Cai, Understanding the role of the porous electrode microstructure in redox flow battery performance using an experimentally validated 3D pore-scale lattice Boltzmann model, J. Power Sources 447 (2020) 227249, doi:10.1016/j.jpowsour.2019.227249.
[32] Q. Ma, Q. Xu, Q. Chen, Z. Chen, H. Su, W. Zhang, Lattice Boltzmann model for complex transfer behaviors in porous electrode of all copper redox flow battery with deep eutectic solvent electrolyte, Appl. Therm. Eng. 160 (2019) 114015, doi:10.1016/j.applthermaleng.2019.114015.
[33] M.D.R. Kok, R. Jervis, T.G. Tranter, M.A. Sadeghi, D.J.L. Brett, P.R. Shearing, J.T. Gostick, Mass transfer in fibrous media with varying anisotropy for flow battery electrodes: direct numerical simulations with 3D X-ray computed tomography, Chem. Eng. Sci. 196 (2019) 104–115, doi:10.1016/j.ces.2018.10.049.
[34] M.A. Sadeghi, M. Aganou, M. Kok, M. Aghighi, G. Merle, J. Barralet, J. Gostick, Exploring the impact of electrode microstructure on redox flow battery performance using a multiphysics pore network model, J. Electrochem. Soc. 166 (2019) A2121–A2130, doi:10.1149/2.0721910jes.

[35] M.D.R. Kok, A. Khalifa, J.T. Gostick, Multiphysics simulation of the flow battery cathode: cell architecture and electrode optimization, J. Electrochem. Soc. 163 (2016) A1408–A1419, doi:10.1149/2.1281607jes.
[36] COMSOL Multiphysics, (n.d.). www.comsol.com.
[37] D.R. Lide, CRC Handbook of Chemistry and Physics, CRC Press, 1995.
[38] J. González-García, P. Bonete, E. Expósito, V. Montiel, A. Aldaz, R. Torregrosa-Maciá, Characterization of a carbon felt electrode: structural and physical properties, J. Mater. Chem. 9 (1999) 419–426, doi:10.1039/a805823g.
[39] R.D. Blevins, Flow-Induced Vibration, 2nd ed., Krieger, Malabar, 2001.
[40] H. Schlichting, K. Gersten, Boundary-Layer Theory, Springer, 2017.
[41] J. Newman, Electrochemical Systems, Prentice-Hall, Inc., Englewood Cliffs, 1973.
[42] B.F. Wishaw, R.H. Stokes, The osmotic and activity coefficients of aqueous solutions of ammonium chloride and ammonium nitrate at 25°, Trans. Faraday Soc. 49 (1953) 27–31, doi:10.1039/TF9534900027.
[43] S.N. Lvov, Introduction to Electrochemical Science and Engineering, 1st ed., CRC Press, Boca Raton, 2015.
[44] COMSOL ABBatteries & Fuel Cells Module User's Guide, 2019 https://doc.comsol.com/5.5/docserver/#!/com.comsol.help.bfc/bfc_ug_electrochem.07.79.html?.
[45] P.V. Danckwerts, Continuous flow systems. Distribution of residence times, Chem. Eng. Sci. 50 (1995) 3855, doi:10.1016/0009-2509(96)81810-0.
[46] A. Nicolle, I. Eames, Numerical study of flow through and around a circular array of cylinders, J. Fluid Mech. 679 (2011) 1–31, doi:10.1017/jfm.2011.77.
[47] C. Liang, G. Papadakis, X. Luo, Effect of tube spacing on the vortex shedding characteristics of laminar flow past an inline tube array: a numerical study, Comput. Fluids. 38 (2009) 950–964, doi:10.1016/j.compfluid.2008.10.005.
[48] P. Chen, Y. Shi, L. Zhang, J. Li, X. Zhu, Q. Fu, Q. Liao, Performance of a thermally regenerative battery with 3D-printed Cu/C composite electrodes: effect of electrode pore size, Ind. Eng. Chem. Res. (2020), doi:10.1021/acs.iecr.0c03937.